Wavelength dependence of high-order harmonic yields in solids

Xi Liu,[1] Liang Li,[1] Xiaosong Zhu,[1,*] Tengfei Huang,[1] Xiaofan Zhang,[1] Dian Wang,[1] Pengfei Lan,[1,†] and Peixiang Lu[1,2]

[1]*School of Physics and Wuhan National Laboratory for Optoelectronics, Huazhong University of Science and Technology, Wuhan 430074, China*

[2]*Hubei Key Laboratory of Optical information and Pattern Recognition, Wuhan Institute of Technology, Wuhan 430205, China*

We theoretically investigate the wavelength dependence of high-order harmonic yields in solids driven by a mid-infrared laser field. By solving the three-dimensional two-band density matrix equations in the wavelength range of 2.0–7.5 μm, it is shown that, in the limit of slow dephasing (dephasing time $T_2 \to \infty$), the high-order harmonic yield from a crystal follows a scaling of λ^{-4} for a fixed energy interval. The λ^{-4} scaling is attributed to the wave-packet spreading (λ^{-3}) for the overall yield and the energy distribution effect (λ^{-1}) due to the increase of the cutoff. For the crystal with a finite dephasing time T_2, we find that the exponential factor x of λ^{-x} increases with a decay of T_2. An apparent and rapid fluctuation on a fine wavelength mesh is also observed in the harmonic yields. The fine-scale oscillation originates from the quantum interference effect, and the corresponding modulation period $\delta\lambda$ scales as λ^{-1}.

I. INTRODUCTION

When matter is irradiated by an intense laser pulse, the laser-matter interaction gives rise to many interesting strong-field phenomena [1–4]. One of the most prominent processes among these phenomena is the high-order harmonic generation (HHG) [5,6]. HHG from gas targets provides an effective route to generate coherent attosecond pulses [7] in the extreme ultraviolet spectral regimes and to explore the electronic structures [8,9] and ultrafast dynamics [10] of atomic and molecular systems. The recent experimental observation [11] of nonperturbative harmonics from bulk ZnO crystal opens up an avenue to study the HHG in solid-state materials. The high density of a crystal target guarantees the superiority of the high conversion efficiency for the solid HHG [12,13]. In addition, the electronic state information of a solid target can imprint itself on the harmonic spectrum [14–16]. Hence the solid HHG provides a useful scheme to reconstruct the energy band structure [17,18] of a crystal with an all-optical method and even to probe the attosecond electronic dynamics [19,20] in condensed matter.

In comparison to atomic or molecular systems, the high density and periodicity of a solid target lead to the distinctly different characteristics in harmonic radiations [21–24], as the laser-driven electrons in solids are always influenced by the periodic potential [12]. For example, the cutoff energy of the solid HHG depends linearly on the field strength [11,25,26] instead of the quadratic dependence in the gas HHG. The emergence of the multiple-plateau structure is also a typical feature of the high-order harmonic spectra from solids [27–29]. The mechanism of the solid HHG is an interesting topic of wide debate. It is generally considered that the solid HHG is contributed by two major channels [30–32]: an intraband current arising from the Bloch oscillation in individual bands and an interband current due to electron transitions between the valence and conduction bands. Currently, some theoretical models and intuitive pictures [32–40] have been built to describe the HHG process in solids.

The scaling law of the harmonic yield on wavelength λ is a fundamental issue of great concern in the attosecond science community [41,42]. For the HHG from rare-gas atoms, theoretical calculations [43–46] and experiment studies [47] reveal a wavelength scaling of λ^{-x} with $5 \leqslant x \leqslant 6$ for a fixed energy interval at a constant intensity. This power law with $x \approx 5$ is ascribed to two contributions [44]: the spreading of the returning wave packet produces a λ^{-3} scaling for the overall yield and the increase of the cutoff energy $E_{\text{cutoff}} \propto \lambda^2$ brings out an additional factor of λ^{-2}. When a finer wavelength mesh is adopted, it is surprisingly found that the harmonic yield does not smoothly decrease with the fundamental wavelength, but exhibits a rapid oscillation, and its modulation period scales as λ^{-2} [45]. The semiclassical analysis based on the strong-field approximation (SFA) reveals that the rapid oscillation stems from the interference effect of the rescattering electron trajectories. As another perspective, Frolov *et al.* [46] attribute the fine-scale oscillation to the quantum threshold phenomena, which are sensitive to the symmetry of the bound-state wave function. However, the wavelength scaling law for the high-order harmonic yield in solids is a recent area of study.

In this work, the wavelength dependence of high-order harmonic yields in solids is investigated by solving the three-dimensional (3D) two-band density matrix equations (DMEs) for the ZnO crystal. The driving wavelengths range from 2.0 to 7.5 μm, i.e., within the mid-infrared (MIR) region [48]. It is found that the harmonic yield for a fixed energy interval follows a λ^{-4} scaling for the crystal with an infinite dephasing time T_2. The origin of the wavelength scaling law in solid

HHG is attributed to the spreading of the wave packet and the increase of the cutoff energy. When the decoherence process is considered, it is shown that the exponential factor x of λ^{-x} increases with the decrease of the dephasing time T_2. The fine-scale oscillation originating from the quantum interference effect is also found in the harmonic spectra. The modulation period of the fine-scale oscillation for solid HHG scales as λ^{-1}, unlike the case of λ^{-2} in gas HHG.

This paper is organized as follows. In Sec. II, we describe the theoretical framework and present the band structure of the solid target in our simulations. In Sec. III, we investigate the wavelength scaling of high-order harmonic yields in the solid target and discuss the influence of the dephasing time on the wavelength scaling. In Sec. IV, the fine-scale oscillation of the harmonic yield and the corresponding modulation period are studied. We summarize our works in Sec. V.

II. THEORETICAL MODEL

In our simulation, the interaction of a strong laser pulse with the ZnO crystal is described by a three-dimensional (3D) two-band model with the tight-binding approximation. Atomic units are used throughout this paper unless otherwise stated. The ZnO crystal has the wurtzite structure and the coordinate directions are chosen as $\mathbf{e}_x || \Gamma - M$, $\mathbf{e}_y || \Gamma - K$, and $\mathbf{e}_z || \Gamma - A$ in our calculation. The dispersion relation of the band m is written as the sum of bands along each individual direction [26], i.e.,

$$E_m(\mathbf{k}) = E_{m,x}(k_x) + E_{m,y}(k_y) + E_{m,z}(k_z), \quad (1)$$

where $m = (v, c)$ stands for the valence and conduction bands, respectively. The band in each direction can be expanded with the Fourier series as

$$E_{v,i}(k_i) = \sum_{j=0}^{\infty} C_{v,i}^j \cos{(jk_i a_i)}, \quad (2)$$

$$E_{c,i}(k_i) = E_g + \sum_{j=0}^{\infty} C_{c,i}^j \cos{(jk_i a_i)}, \quad (3)$$

where $i = (x, y, z)$ stands for three individual axes and $(a_x, a_y, a_z) = (5.32, 6.14, 9.83)$ are the lattice constants in three directions. E_g is the band-gap energy at the Γ point and is given by $E_g = 3.3$ eV in the model. Besides, E_g is also the minimum band-gap energy of the valence band (VB) and the conduction band (CB). The expansion coefficients $C_{v,i}^j$ and $C_{c,i}^j$ are obtained with a nonlocal empirical pseudopotential method for $\Gamma - M$ and the nearest-neighbor expansion for $\Gamma - K$ and $\Gamma - A$. All resulting parameters can be found in Ref. [26]. Figure 1(a) shows the band structures of the valence and conduction bands for $\Gamma - M$ in the reciprocal space. The corresponding energy difference $\epsilon_{g,x}(k_x) = E_{c,x}(k_x) - E_{v,x}(k_x)$ is also presented in Fig. 1(b) with the red solid line. It is worth noting that $\epsilon_{g,x}(k_x)$ depends linearly on k_x approximately as guided by the yellow dashed lines. The approximate linear dependence of the band gap is typical in the current solid HHG studies [30,35,49].
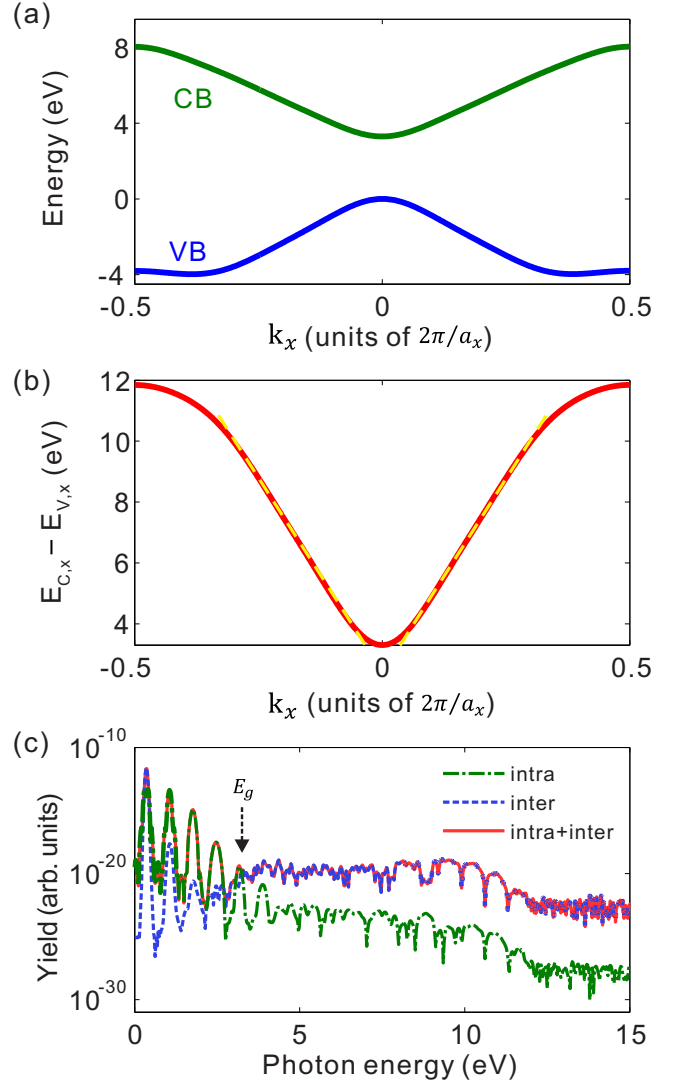

FIG. 1. (a) Band structures and the (b) band gap (red solid line) of conduction and valence bands along the $\Gamma - M$ direction. (c) High harmonic spectra contributed by the intraband, interband, and overall currents. The black arrow indicates the minimum band-gap energy $E_g = 3.3$ eV in panel (c).

The response of the laser-driven electron in a crystal is described by the 3D two-band DMEs [26,32]:

$$\dot{\pi}(\mathbf{K}, t) = -\frac{\pi(\mathbf{K}, t)}{T_2} - i\Omega(\mathbf{K}, t)w(\mathbf{K}, t)e^{-iS(\mathbf{K}, t)}, \quad (4)$$

$$\dot{n}_v(\mathbf{K}, t) = -i\Omega^*(\mathbf{K}, t)\pi(\mathbf{K}, t)e^{iS(\mathbf{K}, t)} + \text{c.c.}, \quad (5)$$

$$\dot{n}_c(\mathbf{K}, t) = i\Omega^*(\mathbf{K}, t)\pi(\mathbf{K}, t)e^{iS(\mathbf{K}, t)} + \text{c.c.}, \quad (6)$$

where n_v and n_c are the populations of the valence and conduction bands, respectively. π is the off-diagonal element of the density matrix. $w = n_v - n_c$ is the population difference between the valence and conduction bands. The crystal momentum $\mathbf{k}$ in the first Brillouin zone (BZ) is shifted with the vector potential $\mathbf{A}(t)$ as $\mathbf{K} = \mathbf{k} - \mathbf{A}(t)$. $\Omega(\mathbf{K}, t)$ is the Rabi frequency and is given by $\Omega(\mathbf{K}, t) = \mathbf{F}(t) \cdot \mathbf{d}[\mathbf{K} + \mathbf{A}(t)]$, where $\mathbf{F}(t)$ is the laser field and $\mathbf{d}(\mathbf{k})$ is the

transition dipole moment. In our simulation, **d** is assumed to be k independent and is chosen as $\mathbf{d} = (3.46, 3.46, 3.94)$. The same treatment can be found in previous works [26,32,50]. $S(\mathbf{K},t)$ is the classical action and is represented as $S(\mathbf{K},t) = \int_{-\infty}^{t} \epsilon_g[\mathbf{K} + \mathbf{A}(\tau)]d\tau$, where $\epsilon_g = E_c - E_v$ is the band gap between the conduction and valence bands. T_2 is the dephasing time stemming from the coherence decay in solids. The DME is equivalent to the semiconductor Bloch equation [51] in the single-electron limit [32].

The HHG in solids is contributed by the intraband current $\mathbf{j}_{ra}$ and the interband current $\mathbf{j}_{er}$, which are given by

$$\mathbf{j}_{ra}(t) = \sum_{m=c,v} \int_{BZ} \mathbf{v}_m[\mathbf{K} + \mathbf{A}(t)]n_m(\mathbf{K},t)d^3\mathbf{K}, \qquad (7)$$

$$\mathbf{j}_{er}(t) = \frac{d}{dt} \int_{BZ} \mathbf{p}(\mathbf{K},t)d^3\mathbf{K}, \qquad (8)$$

respectively. Herein, $\mathbf{v}_m(\mathbf{k}) = \nabla_{\mathbf{k}}E_m(\mathbf{k})$ is the band velocity and $\mathbf{p}(\mathbf{K},t)$ is the polarization given by

$$\mathbf{p}(\mathbf{K},t) = \mathbf{d}[\mathbf{K} + \mathbf{A}(t)]\pi(\mathbf{K},t)e^{iS(\mathbf{K},t)} + \text{c.c.} \qquad (9)$$

The total laser-induced current $\mathbf{j}(t)$ is obtained by $\mathbf{j}(t) = \mathbf{j}_{ra}(t) + \mathbf{j}_{er}(t)$. High-order harmonic spectra contributed by $\mathbf{j}_{ra}$, $\mathbf{j}_{er}$, and $\mathbf{j}(t)$ are calculated by the Fourier transform of the corresponding currents.

The ZnO crystal is irradiated by pulses polarized along the $\Gamma-M$ (x axis) direction. All electrons are initially occupied in the valence band in our simulation. The Gaussian envelope with a full width at half maximum of 40 fs and a total duration of 180 fs is adopted for all laser pulses. The carrier-envelope phase (CEP) is fixed as $\phi = 0°$. The laser wavelengths adopted are within the MIR region and range from 2.0 to 7.5 μm. Figure 1(c) shows the harmonic spectra contributed by the intraband, interband, and overall (intraband + interband) currents, where the black arrow indicates the position of the minimum band-gap energy $E_g = 3.3$ eV. The laser wavelength is 3.5 μm and the laser intensity is 3.2×10^{11} W/cm^2. The dephasing time is chosen as $T_2 = \infty$. One can see clearly that the intraband processes are dominant for harmonics with photon energies below the minimum band-gap energy E_g, whereas the interband processes dominate the higher-order harmonics spanning the plateau region. This is in agreement with the previous conclusion that the observed harmonic spectrum is separated into the below-threshold region (dominated by the intraband mechanism) and the plateau region (dominated by the interband mechanism) by the minimum band gap for MIR driver pulses [30,32,34,37]. The harmonic plateaus shown in Fig. 1(c) are somewhat noisy and some harmonics cannot be recognized clearly in the spectra. This is because the absence of dephasing time, i.e., $T_2 = \infty$, masks the clean odd harmonics in the plateau as has been pointed out in Ref. [32]. A clearer harmonic spectrum can be obtained if a finite dephasing time T_2 is adopted in our simulation.

The study of wavelength scaling law focuses on the harmonic yield per unit energy range and unit time in the harmonic plateau. This average harmonic yield is denoted as ΔI. In this work, the total duration of the laser pulses is fixed as 180 fs. The energy range is fixed at 4 to 8 eV. Thus, the harmonic yield ΔI can be calculated by integrating the power spectrum of the harmonic radiations, i.e.,

$$\Delta I = \int_{4\,\text{eV}}^{8\,\text{eV}} |\mathbf{j}(\omega)|^2 d\omega. \qquad (10)$$

The fact that the harmonic plateau always starts from $E_g = 3.3$ eV guarantees that the lower bound of 4 eV in Eq. (10) is always located in the plateau region. The upper bound in Eq. (10) is chosen as 8 eV because we have verified that it does not exceed the cutoff energies of the harmonics for all adopted laser pulses. Thus the integration interval (4 to 8 eV) is always located in the plateau of the harmonic spectrum. Considering that the harmonic yields in plateau regions are nearly equal, any energy range can be chosen as the integration interval as long as it is in the plateau region. Thus our conclusions are independent of the chosen energy range in the harmonic plateau.

III. WAVELENGTH SCALING IN HHG YIELD

Our study aims to reveal the HHG yield in solids as a function of the driving wavelength at a constant intensity. It has been widely accepted that the harmonic yield in gas follows a wavelength scaling law of λ^{-x} [6,43–47]. Thus we adopt a power law with the form

$$\Delta I = \beta\lambda^{-x} \qquad (11)$$

to fit the relation using the sample wavelength λ and the corresponding harmonic yield ΔI. In Eq. (11), we take its logarithm and it reads

$$\ln\Delta I = \ln\beta - x\ln\lambda. \qquad (12)$$

In order to evaluate the value and uncertainty of x, a least-squares method is used to fit the equation using calculated $\ln\Delta I$ and $\ln\lambda$ in Eq. (12). The uncertainty Δx of x is obtained by solving the 95% confidence interval $(x - \Delta x, x + \Delta x)$ with the assumption that it obeys the normal distribution. The correlation coefficient r is also obtained to evaluate the goodness of the fit. The detailed calculation procedure for x, Δx, and r can be found in the Appendix.

Figures 2(a)–2(c) show the harmonic yield ΔI as a function of the driving wavelength λ in double logarithmic coordinates with the laser intensities fixed at 2.2×10^{11}, 3.2×10^{11}, and 4.2×10^{11} W/cm^2, respectively. The dephasing effect is neglected provisionally, i.e., dephasing time $T_2 = \infty$. The driving wavelength ranges from 2.0 to 7.5 μm and the wavelength spacing is 250 nm. One can see clearly that the sample points agree with the fitting straight-lines very well in the double logarithmic coordinate. The correlation coefficients for the three intensities are -0.9965, -0.9979, and -0.9934, respectively. The fact that all three correlation coefficients are very close to -1 suggests that $\ln\Delta I$ is highly negative correlative to $\ln\lambda$, i.e., $\Delta I \propto \lambda^{-x}$. The fitted exponents x with their uncertainties Δx are 3.98 ± 0.15, 4.07 ± 0.12, and 4.10 ± 0.21, respectively. One can see clearly that all three fitted x values are very close to 4. Considering the uncertainty Δx, the value of 4 is always located in the 95% confidence interval $(x - \Delta x, x + \Delta x)$. Therefore, the harmonic yield should follow a λ^{-4} scaling. The wavelength scaling of λ^{-4} in solids is distinctly different from that of $\lambda^{-(5-6)}$ in gases.
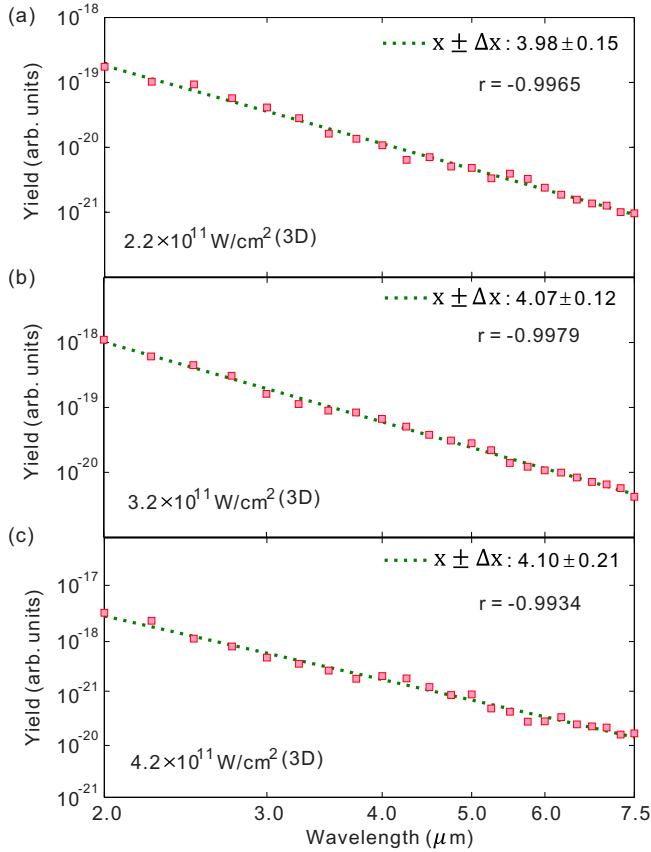
FIG. 2. Wavelength dependence of the harmonic yield ΔI for the laser intensities of (a) 2.2×10^{11} W/cm^2, (b) 3.2×10^{11} W/cm^2, and (c) 4.2×10^{11} W/cm^2, respectively. The results are obtained by solving the 3D two-band DME. The double logarithmic coordinates are adopted in panels (a)–(c).

In order to clarify the mechanism of λ^{-4} scaling in solid HHG, we investigate the wavelength scaling of the harmonic yield from ZnO crystal in reduced dimensions. Figures 3(a)–3(c) show the harmonic yields as a function of the driving wavelength in the double logarithmic coordinates by solving the 2D two-band DME. The laser intensities adopted are the same as those in Figs. 2(a)–2(c). One can see that the power-law distribution still satisfies because all three correlation coefficients (-0.9953, -0.9938, and -0.9903) are very close to -1. The fitted exponents x with uncertainties Δx are 2.89 ± 0.16, 2.96 ± 0.13, and 2.91 ± 0.19, respectively. The obtained three exponents equaling approximately to 3 indicate that the harmonic yield follows a λ^{-3} scaling in a 2D system. Likewise, the harmonic yields calculated by the 1D two-band DME are shown in Figs. 3(d)–3(f). It is found that the three fitted exponents (1.95 ± 0.13, 2.06 ± 0.18, and 1.98 ± 0.15) are very close to 2 within the 95% confidence interval, which suggests that the harmonic yield follows a λ^{-2} scaling in a 1D system. The correlation between $\ln \Delta I$ and $\ln \lambda$ is still very significant because the correlation coefficients -0.9901, -0.9872, and -0.9876 are very close to -1. The wavelength scalings obtained from 3D (λ^{-4}), 2D (λ^{-3}), and 1D (λ^{-2}) models suggest that the exponential factor x of λ^{-x} will fall off by 1 if the dimensionality of a system is

reduced by 1. This is clear evidence that the wavelength scaling can be contributed by the wave-packet spreading. The wave-packet spreading gives rise to a λ^{-1} scaling in each dimension, which constitutes the λ^{-3} scaling for the real 3D system.

The interband HHG in solids can be described by the electron-hole recollision model [32,52], which is similar to the three-step process in gas HHG. Specifically, the laser-driven electron tunnels from the valence band first, the electron-hole pair is subsequently accelerated in valence and conduction bands in the laser field, and finally the laser-driven electron recombines with the hole accompanied by the harmonic radiations. The propagations of the electron-hole pair in valence and conduction bands will result in the spreading of the wave packet. Similarly to the gas HHG, the spreading of the wave packet leads to a λ^{-3} scaling for the overall yield.

Many studies have verified that the cutoff energy of the ZnO crystal is linearly dependent on the laser wavelength in the MIR regime. For example, Vampa *et al.* [26] pointed out that the cutoff energy of the ZnO crystal (denote as E_{cutoff}) is proportional to A_0, i.e.,

$$E_{\mathrm{cutoff}} \propto A_0, \tag{13}$$

where A_0 is the amplitude of the vector potential. The linear dependence of the cutoff energy on A_0 is attributed to the fact that the energy gap of the conduction and valence bands (denote as ϵ_g) is approximately a linear function of the crystal momentum k in the positive k axis [see Fig. 1(b)] [35], namely,

$$\epsilon_g(k) \propto k. \tag{14}$$

The semiclassical motion equation $k(t) = k_0 + A(t)$ suggests that

$$k(t) \propto A(t). \tag{15}$$

Combining Eqs. (14) and (15), Eq. (13) can be obtained by [35]

$$E_{\mathrm{cutoff}} = \max\{\epsilon_g[k(t)]\} \propto \max[k(t)]$$
$$\propto \max[A(t)] = A_0. \tag{16}$$

Therefore, as in the case of the gas HHG, the extension of the cutoff energy $E_{\mathrm{cutoff}} \propto \lambda$ results in an additional factor λ^{-1} in the wavelength scaling for a fixed energy interval. Our results reveal that the λ^{-4} scaling for the solid HHG is contributed by the spreading of the wave packet (λ^{-3}) for the overall yield and the increase of the cutoff energy (λ^{-1}). It is worth noting that the relation $\max[A(t)] = A_0$ may not precisely hold especially for the long wavelengths because the laser pulse contains only a few optical cycles. However, we have verified that the relative error rates of $\max[A(t)]$ and A_0 are less than 5% for the laser pulses adopted in this work. Thus, the duration of adopted laser pulses is enough long and the relation $\max[A(t)] = A_0$ is still valid in our research. In fact, further investigations reveal that the wavelength scaling law is not distinctly affected by the CEP effect for the chosen laser pulses in this work.
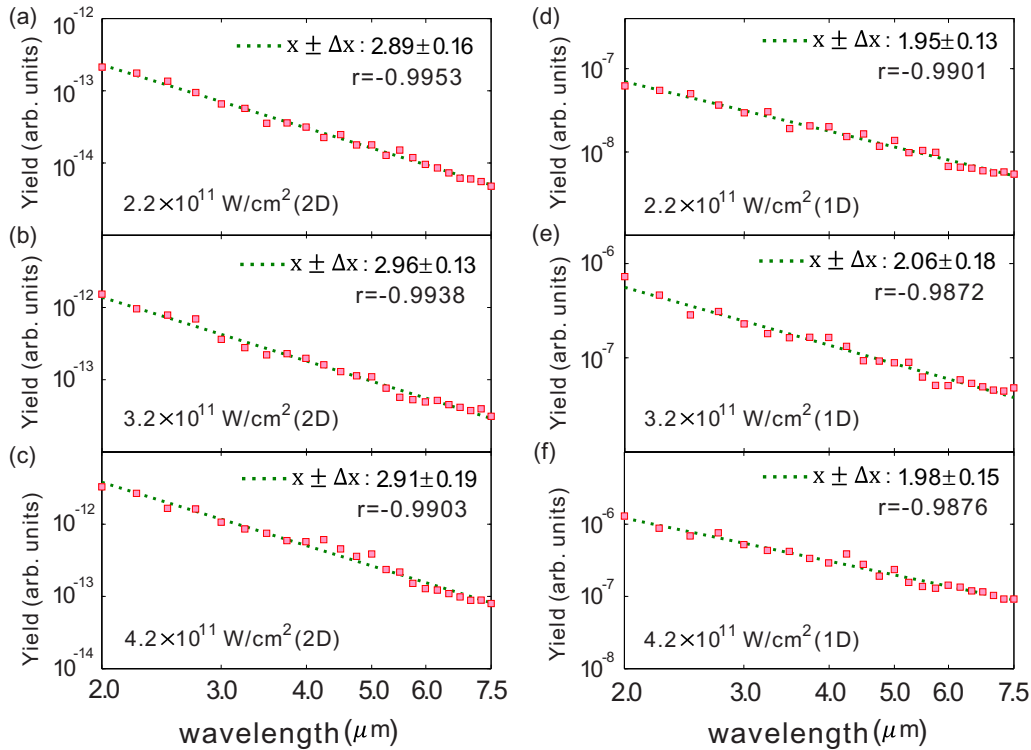
FIG. 3. Wavelength dependence of the harmonic yield ΔI by solving the two-band 2D [panels (a)–(c)] and 1D [panels (d)–(f)] DMEs. The laser intensities are same as those in Figs. 2(a)–2(c). The double logarithmic coordinates are adopted in panels (a)–(f).

The wavelength scaling for the solid harmonic yield will change when the decoherence process is taken into account. Figures 4(a) and 4(b) show the exponential factor x of λ^{-x} as a function of the dephasing time T_2. Here the laser intensity is fixed at $3.2 \times 10^{11}\,\mathrm{W/cm^2}$. One can see that the exponential factor x decreases rapidly with the increasing T_2 in the region of the short dephasing time. When T_2 is long enough, as indicated by the horizontal dashed line in Fig. 4(b), x approaches asymptotically the limiting value $x = 4.07$, which corresponds to the case of $T_2 = \infty$. A logarithmic coordinate is adopted for the T_2 axis in Fig. 4(b) considering the extremely slow decay of x in the corresponding region. Our results reveal that the dephasing time plays an important role in the wavelength scaling for the solid HHG yield. In solids, the dephasing time is due to the inelastic scattering by lattices and the electron-electron interaction. The decay

of x with increasing T_2 suggests that the dissipations arising from the decoherence effect in solids will further suppress the harmonic yield for a longer wavelength. The suppression of the harmonic yield due to the dephasing can be intuitively understood by the viewpoint that dissipations in solids damp out the electronic interband transitions, which are the origin of the interband HHG in solids.

IV. FINE-SCALE OSCILLATIONS

The harmonic yields shown in Figs. 2(a)–2(c) and Figs. 3(a)–3(f) exhibit another feature that the harmonic efficiencies do not vary smoothly but slightly fluctuate with the increasing λ like in gas HHG. In order to explore the fluctuations of the harmonic yields in detail, a much finer wavelength mesh with the spacing of 10 nm is adopted to investigate the harmonic yields. It is found that the fine-scale oscillations of the harmonic yields on wavelength also appear in solids. We choose three wavelength regions to demonstrate the fine-scale oscillations on λ in the HHG yield. Figures 5(a)–5(c) show the HHG yields in the regions of 2.5–3.3, 3.4–3.8, and 5.4–5.8 μm, respectively. The laser intensity is $3.2 \times 10^{11}\,\mathrm{W/cm^2}$. From Figs. 5(a)–5(c), one can see clearly that the harmonic yield exhibits a fluctuation behavior with the alternating peaks and valleys. The oscillation periods $\delta\lambda$ for three wavelength regions are different and approximately equal to 160, 100, and 80 nm, respectively.

In gas HHG, the origin of a fine-scale oscillation in harmonic yield is attributed to the quantum path interference [45]. Specifically, based on the SFA model, the time-
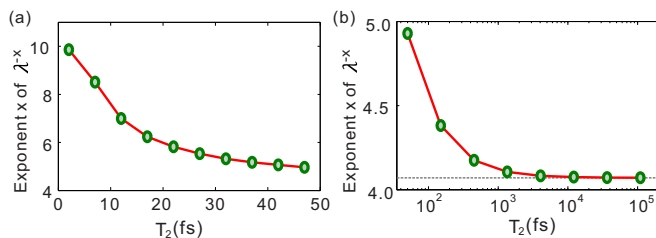

FIG. 4. The exponential factor x as a function of the dephasing time T_2 in the ranges of (a) 0–50 fs and (b) 50–2×10^5 fs. The logarithmic coordinate is adopted for the T_2 axis in panel (b). The horizontal dashed line indicates the x value in the case of $T_2 = \infty$.
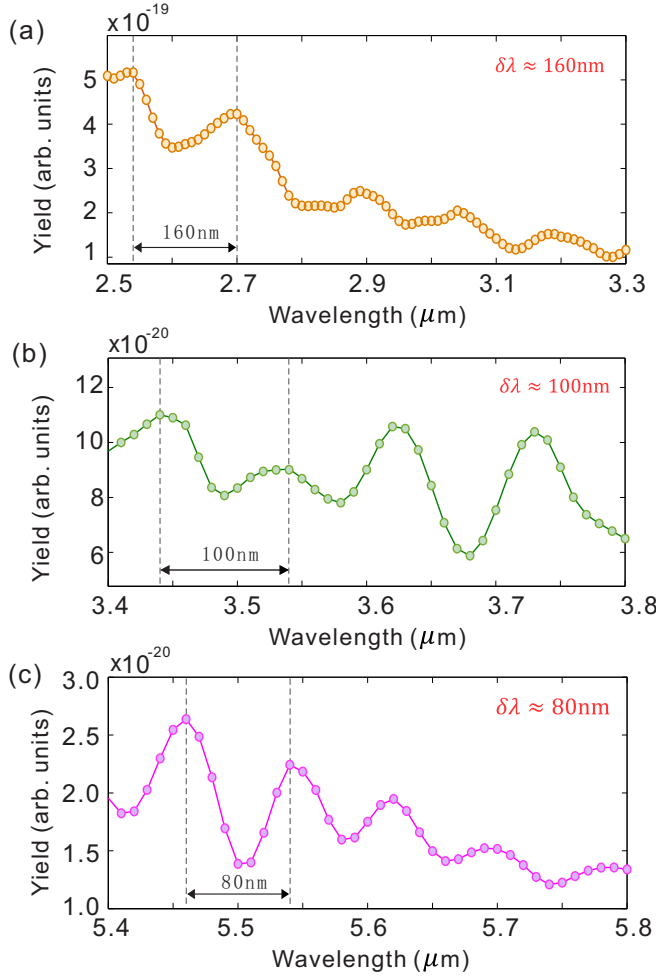
FIG. 5. Harmonic yield as a function of the laser wavelength with the spacing of 10 nm in the regions of (a) 2.5–3.3 μm, (b) 3.4–3.8 μm, and (c) 5.4–5.8 μm. The laser intensity is fixed at $3.2 \times 10^{11}\,\mathrm{W/cm^2}$.

dependent dipole moment can be expressed as [6]

$$\mathbf{x}(t) = i \int_{-\infty}^{t} dt' \int d^3\mathbf{p} \cdot \mathbf{d}^*[\mathbf{p} - \mathbf{A}(t)]$$
$$\times \mathbf{F}(t') \cdot \mathbf{d}[\mathbf{p} - \mathbf{A}(t')]e^{-iS(\mathbf{p},t',t)} + \text{c.c.}, \quad (17)$$

where $S(\mathbf{p}, t', t) = \int_{t'}^{t} \{[\mathbf{p} - \mathbf{A}(t'')]^2/2 + I_p\}dt''$ is the semiclassical action and I_p is the ionization potential. As has been pointed out in Ref. [45], the interference oscillations in harmonic yields for the gas HHG are controlled by the evolution phase of the time-dependent dipole moment, i.e., the semiclassical action $S(\mathbf{p}, t', t)$. By using the Keldysh approximation $w(t) \approx 1$, the interband current can be written as [32]

$$\mathbf{j}_{\mathrm{er}}(t) = \frac{d}{dt} \int_{-\infty}^{t} dt' \int_{\mathrm{BZ}} d^3\mathbf{k} \cdot \mathbf{d}(\mathbf{k})e^{-(t-t')/T_2}$$
$$\times \mathbf{F}(t') \cdot \mathbf{d}^*[\kappa(t')]e^{-iS(\mathbf{k},t',t)} + \text{c.c.}, \quad (18)$$

where $\kappa(t') = \mathbf{k} + \mathbf{A}(t') - \mathbf{A}(t)$, and the classical action $S(\mathbf{k}, t', t) = \int_{t'}^{t} \epsilon_g[\kappa(\tau)]d\tau$. From Eq. (18), one can see that the evolution phase of the interband current in solids is controlled by the classical action $S(\mathbf{k}, t', t)$. The concept

of quantum trajectories in solid HHG has been built by the electron-hole recollision model [26,52]. By comparing Eqs. (17) and (18), it can be concluded that the evolution phase $S(\mathbf{k}, t', t)$ in solids also will lead to the similar interference oscillations in harmonic yields due to the interference effects of quantum trajectories as in the case of the gas HHG. Therefore, the fine-scale oscillations presented in solid HHG yields are also due to the interference effects of quantum trajectories.

The oscillation period $\delta\lambda$ for the solid HHG can be deduced using a similar method as in the gas case. When the saddle-point integration is introduced in Eq. (18), the classical action S can be written as $S(k, t_i, t_f) = \int_{t_i}^{t_f} \epsilon_g[\kappa(\tau)]d\tau$, where the bounds of the integration are the ionization time t_i and the recombination time t_f of the electron (or hole). Considering Eq. (14) and the relation $\kappa(\tau) = k + A(\tau) - A(t_f)$, it is found that $\epsilon_g[\kappa(\tau)] \propto \kappa(\tau) \propto A(\tau) = F_0/\omega_0 \sin(\omega_0\tau)$. Thus,

$$\overline{S} = \overline{\int_{t_i}^{t_f} \epsilon_g[\kappa(\tau)]d\tau} \propto \overline{\int_{t_i}^{t_f} \frac{F_0}{\omega_0} \sin(\omega_0\tau)d\tau}$$
$$= \frac{F_0}{\omega_0^2}\overline{\cos(\omega_0 t_i) - \cos(\omega_0 t_f)} \propto \lambda^2. \quad (19)$$

That is, $\overline{S}$ scales as λ^2. Considering that the interference oscillation is induced by the evolution phase $S(k, t_i, t_f)$, the modulation period of the oscillation corresponds to a phase change of $\overline{S}$ by 2π [45]. Therefore,

$$2\pi = \delta\overline{S} = \frac{d\overline{S}}{d\lambda}\delta\lambda. \quad (20)$$

According to Eq. (19), we obtain

$$\frac{d\overline{S}}{d\lambda} \propto \lambda. \quad (21)$$

Based on Eqs. (20) and (21), it can be concluded that

$$\delta\lambda \propto \lambda^{-1}. \quad (22)$$

This result suggests that the oscillation period of the harmonic yield on wavelength is not a constant but is dependent on the wavelength itself. The derivation of λ^{-1} scaling for the oscillation period $\delta\lambda$ further verifies that fine-scale oscillations in solid HHG originate from the quantum interference effects.

In order to verify Eq. (22), we extract the oscillation period $\delta\lambda$ from the harmonic yields obtained by solving the 3D two-band DME. Then $\delta\lambda$ and λ are fitted with the form of $\delta\lambda = \alpha\lambda^{-x}$. Here the value and uncertainty of the exponent x are calculated with the same procedures as those in Eq. (11). Figure 6 shows the oscillation period $\delta\lambda$ as a function of λ for the wavelength ranging from 2.0 to 7.5 μm in the double logarithmic coordinate. One can see that the distribution of sample points follow the fitting straight-line in the double logarithmic coordinate. The correlation coefficient $r = -0.9816$ suggests that the correlation between $\ln\delta\lambda$ and $\ln\lambda$ is quite significant. The fitted x with its uncertainty is 1.06 ± 0.15. This is in good agreement with the theoretical prediction of 1, very well within the uncertainty of fit. It is worth noting that the deductions shown previously are not confined in the 3D system. Thus, the fine-scale oscillations in harmonic yield
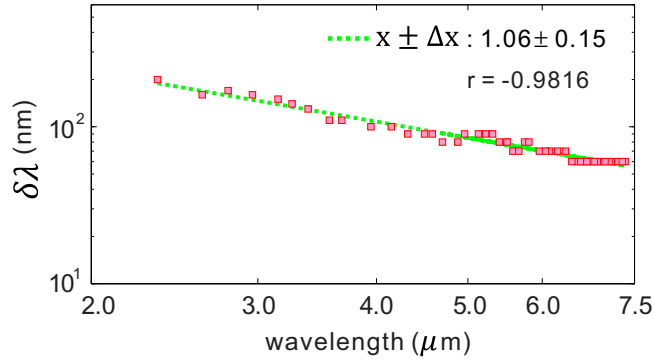
FIG. 6. The oscillation period $\delta\lambda$ as a function of the driving wavelength λ. The laser intensity is 3.2×10^{11} W/cm^2. The double logarithmic coordinate is adopted.

can also be observed in the reduced dimensionality (1D and 2D) systems with the same scaling laws as the case of the 3D system. This conclusion has been verified numerically by solving the 2D and 1D two-band DMEs.

The above discussions are focused on the prototype of bulk ZnO crystal. When the band structure of a crystal satisfies $\epsilon_g(k) \propto k^n$ ($n = 1$ for the ZnO crystal specifically), Eq. (16) should be revised as $E_{\mathrm{cutoff}} \propto (A_0)^n$. The wavelength scaling of the HHG yield due to the wave-packet spreading and the increase of the cutoff becomes $\Delta I \propto \lambda^{-(3+n)}$. Similarly, the scaling of the oscillation period shown in Eq. (22) should be obtained as $\delta\lambda \propto \lambda^{-n}$. The gas HHG originates from the electronic transitions from the free state ($E_c = k^2/2$, the crystal momentum k degenerates into the mechanical momentum p in this case) to the ground state ($E_v = -I_p$, I_p is the ionization potential). Thus, the scalings of $\Delta I \propto \lambda^{-5}$ in the gas harmonic yield and $\delta\lambda \propto \lambda^{-2}$ in the fine-scale oscillation can be directly obtained according to $\epsilon_g = k^2/2 + I_p \propto k^2$. Table I summarizes the wavelength dependencies of ΔI and $\delta\lambda$ for the ZnO crystal, the gas system, and the matter satisfying the relation $\epsilon_g(k) \propto k^n$ (called the k^n-type matter). One can see that the wavelength dependencies of ΔI and $\delta\lambda$ are entirely determined by the exponential factor n in the equation $\epsilon_g(k) \propto k^n$ for both gas and solid HHG. This result reveals that the different wavelength scalings of the harmonic yield and the oscillation period for gases and solids are essentially attributed to the different dependencies of the energy gap ϵ_g on the crystal momentum k.

V. CONCLUSION

In summary, we investigate the wavelength dependence of the harmonic yield in solids driven by MIR laser pulses. It

TABLE I. Wavelength dependencies for the harmonic yield and the oscillation period of the fine-scale oscillation.

Species	$\epsilon_g \propto$	$\Delta I \propto$	$\delta\lambda \propto$
ZnO crystal	k	$\lambda^{-(3+1)}$	λ^{-1}
Gas system	k^2	$\lambda^{-(3+2)}$	λ^{-2}
k^n-type matter	k^n	$\lambda^{-(3+n)}$	λ^{-n}

turns out that the wavelength scaling in solid HHG differs from the case in gas HHG. Nevertheless, the wavelength scaling for solid HHG is contributed by mechanisms similar to those for the gas HHG. Specifically, the yield of solid HHG in MIR laser fields exhibits a λ^{-4} scaling for a fixed energy interval in the absence of dephasing effects. The λ^{-4} scaling originates from the wave-packet spreading for the overall yield (λ^{-3}) and the increase of the cutoff (λ^{-1}). Moreover, the decoherence process is found to have a remarkable impact on the wavelength scaling. The harmonic yield in solids decreases more rapidly when the dephasing is considered. The fine-scale oscillations in harmonic yield due to the quantum interference can be found in solids. Theoretical analysis and numerical simulation indicate that the oscillation period scales as λ^{-1}. Our work also further reveals that the different wavelength scalings and oscillation periods for the gas and solid HHG essentially originate from the different energy-gap equations on crystal momentum.

APPENDIX: THE LEAST-SQUARES FIT AND ITS UNCERTAINTY

In this Appendix, we illustrate the detailed procedure to fit Eq. (12) with the least-squares method. For the given simple data pairs [(x_i, y_i), $i = 1, ..., n$], the goal is to fit them with the form

$$y = a + bx. \tag{A1}$$

According to the least-squares method, the parameter b is calculated by

$$b = \frac{\sum_{i=1}^n (x_i - \bar{x})(y_i - \bar{y})}{\sum_{i=1}^n (x_i - \bar{x})^2}, \tag{A2}$$

where $\bar{x}$ and $\bar{y}$ are the mean values of x and y, respectively. The parameter a is obtained by

$$a = \bar{y} - b\bar{x}. \tag{A3}$$

The correlation coefficient r is given by

$$r = \frac{\sum_{i=1}^n (x_i - \bar{x})(y_i - \bar{y})}{\sqrt{\sum_{i=1}^n (x_i - \bar{x})^2}\sqrt{\sum_{i=1}^n (y_i - \bar{y})^2}}. \tag{A4}$$

The standard deviation of b is denoted as σ_b and is calculated by

$$\sigma_b = \sqrt{\frac{\sum_{i=1}^n (Y_i - y_i)^2}{(n-2)\sum_{i=1}^n (x_i - \bar{x})^2}}, \tag{A5}$$

where $Y_i = a + bx_i$. The 95% confidence interval ($b - \Delta b$, $b + \Delta b$) is obtained by assuming that it obeys the normal

distribution and searching the Δb satisfying the integration

$$\int_{b-\Delta b}^{b+\Delta b} \frac{1}{\sqrt{2\pi}\sigma_b} \exp\left[-\frac{(x-b)^2}{2\sigma_b^2}\right] dx = 0.95. \quad \text{(A6)}$$

In Eq. (12), we choose $\ln \lambda_i = x_i$ and $\ln \Delta I_i = y_i$ in our fitting procedure, where λ_i is the sample wavelength and ΔI_i is the corresponding harmonic yield.

[1] F. Krausz and M. Ivanov, Rev. Mod. Phys. **81**, 163 (2009).

[2] S. Chelkowski, A. D. Bandrauk, and P. B. Corkum, Phys. Rev. Lett. **113**, 263005 (2014).

[3] N. Teeny, E. Yakaboylu, H. Bauke, and C. H. Keitel, Phys. Rev. Lett. **116**, 063003 (2016); B. Wang, L. He, F. Wang, H. Yuan, X. Zhu, P. Lan, and P. Lu, Phys. Rev. A **97**, 013417 (2018); H. Yuan *et al.*, Opt. Lett. **43**, 931 (2018).

[4] L. He, P. Lan, A.-T. Le, B. Wang, B. Wang, X. Zhu, P. Lu, and C. D. Lin, Phys. Rev. Lett. **121**, 163201 (2018); D. Wang, X. Zhu, L. Li, X. Zhang, X. Liu, P. Lan, and P. Lu, Phys. Rev. A **98**, 053410 (2018); X. Ma *et al.*, Opt. Laser Technol. **108**, 235 (2018).

[5] P. B. Corkum, Phys. Rev. Lett. **71**, 1994 (1993).

[6] M. Lewenstein, P. Balcou, M. Y. Ivanov, A. L'Huillier, and P. B. Corkum, Phys. Rev. A **49**, 2117 (1994).

[7] M. Hentschel, R. Kienberger, Ch. Spielmann, G. A. Reider, N. Milosevic, T. Brabec, P. Corkum, U. Heinzmann, M. Drescher, and F. Krausz, Nature (London) **414**, 509 (2001).

[8] J. Itatani, J. Levesque, D. Zeidler, H. Niikura, H. Pépin, J. C. Kieffer, P. B. Corkum, and D. M. Villeneuve, Nature (London) **432**, 867 (2004).

[9] S. Haessler, J. Caillat, W. Boutu, C. Giovanetti-Teixeira, T. Ruchon, T. Auguste, Z. Diveki, P. Breger, A. Maquet, B. Carré, R. Taïeb, and P. Salières, Nat. Phys. **6**, 200 (2010).

[10] W. Li, X. Zhou, R. Lock, S. Patchkovskii, A. Stolow, H. C. Kapteyn, and M. M. Murnane, Science **322**, 1207 (2008).

[11] S. Ghimire, A. D. DiChiara, E. Sistrunk, P. Agostini, L. F. DiMauro, and D. A. Reis, Nat. Phys. **7**, 138 (2011).

[12] Y. S. You, Y. Yin, Y. Wu, A. Chew, X. Ren, F. Zhuang, S. Gholam-Mirzaei, M. Chini, Z. Chang, and S. Ghimire, Nat. Commun. **8**, 724 (2017).

[13] N. Tancogne-Dejean, O. D. Mücke, F. X. Kärtner, and A. Rubio, Phys. Rev. Lett. **118**, 087403 (2017).

[14] S. Jiang, H. Wei, J. Chen, C. Yu, R. Lu, and C. D. Lin, Phys. Rev. A **96**, 053850 (2017).

[15] E. N. Osika, A. Chacón, L. Ortmann, N. Suárez, J. A. Pérez-Hernández, B. Szafran, M. F. Ciappina, F. Sols, A. S. Landsman, and M. Lewenstein, Phys. Rev. X **7**, 021017 (2017).

[16] Y. S. You, D. A. Reis, and S. Ghimire, Nat. Phys. **13**, 345 (2017).

[17] G. Vampa, T. J. Hammond, N. Thiré, B. E. Schmidt, F. Légaré, C. R. McDonald, T. Brabec, D. D. Klug, and P. B. Corkum, Phys. Rev. Lett. **115**, 193603 (2015).

[18] A. A. Lanin, E. A. Stepanov, A. B. Fedotov, and A. M. Zheltikov, Optica **4**, 516 (2017).

[19] M. Schultze, K. Ramasesha, C. D. Pemmaraju, S. A. Sato, D. Whitmore, A. Gandman, J. S. Prell, L. J. Borja, D. Prendergast, K. Yabana, D. M. Neumark, and S. R. Leone, Science **346**, 1348 (2014).

[20] S. Jiang, C. Yu, G. Yuan, T. Wu, Z. Wang, and R. Lu, J. Phys.: Condens. Matter **29**, 275702 (2017).

[21] G. Ndabashimiye, S. Ghimire, M. Wu, D. A. Browne, K. J. Schafer, M. B. Gaarde, and D. A. Reis, Nature (London) **534**, 520 (2016).

[22] N. Tancogne-Dejean, O. D. Mücke, F. X. Kärtner, and A. Rubio, Nat. Commun. **8**, 745 (2017).

[23] U. Huttner, K. Schuh, J. V. Moloney, and S. W. Koch, J. Opt. Soc. Am. B **33**, C22 (2016).

[24] O. D. Mücke, Phys. Rev. B **84**, 081202 (2011).

[25] X. Liu, X. Zhu, X. Zhang, D. Wang, P. Lan, and P. Lu, Opt. Express **25**, 29216 (2017).

[26] G. Vampa, C. R. McDonald, G. Orlando, P. B. Corkum, and T. Brabec, Phys. Rev. B **91**, 064302 (2015).

[27] M. Wu, S. Ghimire, D. A. Reis, K. J. Schafer, and M. B. Gaarde, Phys. Rev. A **91**, 043839 (2015).

[28] K. K. Hansen, T. Deffge, and D. Bauer, Phys. Rev. A **96**, 053418 (2017).

[29] G. R. Jia, X. H. Huang, and X. B. Bian, Opt. Express **25**, 23654 (2017).

[30] P. G. Hawkins, M. Y. Ivanov, and V. S. Yakovlev, Phys. Rev. A **91**, 013405 (2015); C. R. McDonald, G. Vampa, P. B. Corkum, and T. Brabec, *ibid.* **92**, 033845 (2015).

[31] S. Ghimire, A. D. DiChiara, E. Sistrunk, G. Ndabashimiye, U. B. Szafruga, A. Mohammad, P. Agostini, L. F. DiMauro, and D. A. Reis, Phys. Rev. A **85**, 043836 (2012).

[32] G. Vampa, C. R. McDonald, G. Orlando, D. D. Klug, P. B. Corkum, and T. Brabec, Phys. Rev. Lett. **113**, 073901 (2014).

[33] T. Tamaya, A. Ishikawa, T. Ogawa, and K. Tanaka, Phys. Rev. Lett. **116**, 016601 (2016).

[34] M. Wu, D. A. Browne, K. J. Schafer, and M. B. Gaarde, Phys. Rev. A **94**, 063403 (2016).

[35] T. Y. Du and X. B. Bian, Opt. Express **25**, 151 (2017).

[36] T. Y. Du, X. H. Huang, and X. B. Bian, Phys. Rev. A **97**, 013403 (2018).

[37] X. Liu, X. Zhu, P. Lan, X. Zhang, D. Wang, Q. Zhang, and P. Lu, Phys. Rev. A **95**, 063419 (2017).

[38] T. Ikemachi, Y. Shinohara, T. Sato, J. Yumoto, M. Kuwata-Gonokami, and K. L. Ishikawa, Phys. Rev. A **95**, 043416 (2017).

[39] L. Liu, J. Zhao, W. Dong, J. Liu, Y. Huang, and Z. Zhao, Phys. Rev. A **96**, 053403 (2017).

[40] D. Bauer and K. K. Hansen, Phys. Rev. Lett. **120**, 177401 (2018).

[41] P. Colosimo, G. Doumy, C. I. Blaga, J. Wheeler, C. Hauri, F. Catoire, J. Tate, R. Chirla, A. M. March, G. G. Paulus, H. G. Muller, P. Agostini, and L. F. DiMauro, Nat. Phys. **4**, 386 (2008).

[42] K. L. Ishikawa, E. J. Takahashi, and K. Midorikawa, Phys. Rev. A **80**, 011807 (2009).

[43] J. Tate, T. Auguste, H. G. Muller, P. Salières, P. Agostini, and L. F. DiMauro, Phys. Rev. Lett. **98**, 013901 (2007).

[44] A. T. Le, H. Wei, C. Jin, V. N. Tuoc, T. Morishita, and C. D. Lin, Phys. Rev. Lett. **113**, 033001 (2014).

[45] K. Schiessl, K. L. Ishikawa, E. Persson, and J. Burgdörfer, Phys. Rev. Lett. **99**, 253903 (2007).

[46] M. V. Frolov, N. L. Manakov, and A. F. Starace, Phys. Rev. Lett. **100**, 173001 (2008).

[47] A. D. Shiner, C. Trallero-Herrero, N. Kajumba, H. C. Bandulet, D. Comtois, F. Légaré, M. Giguère, J-C. Kieffer, P. B. Corkum, and D. M. Villeneuve, Phys. Rev. Lett. **103**, 073902 (2009).

[48] U. Elu *et al.*, Optica **4**, 1024 (2017); Q. Liu *et al.*, Opt. Quantum Electron. **50**, 356 (2018); S. Ke *et al.*, *ibid.* **50**, 393 (2018).

[49] L. A. Chizhova, F. Libisch, and J. Burgdörfer, Phys. Rev. B **95**, 085436 (2017).

[50] C. Liu, Y. Zheng, Z. Zeng, and R. Li, Phys. Rev. A **93**, 043806 (2016).

[51] C. Yu, X. Zhang, S. Jiang, X. Cao, G. Yuan, T. Wu, L. Bai, and R. Lu, Phys. Rev. A **94**, 013846 (2016).

[52] G. Vampa and T. Brabec, J. Phys. B: At., Mol. Opt. Phys. **50**, 083001 (2017).